

See discussions, stats, and author profiles for this publication at: <https://www.researchgate.net/publication/309271124>

# The Effect of Gap Flow on Vortex-Induced Vibration of Side-by-Side Cylinder Arrangement

Conference Paper · June 2016

DOI: 10.1115/OMAE2016-54736

---

CITATIONS

2

READS

51

2 authors, including:



Bin Liu

Newcastle University

12 PUBLICATIONS 134 CITATIONS

[SEE PROFILE](#)

## THE EFFECT OF GAP FLOW ON VORTEX-INDUCED VIBRATION OF SIDE-BY-SIDE CYLINDER ARRANGEMENT

**Bin Liu**

Department of Mechanical Engineering  
National University of Singapore  
Singapore  
Email: mpelbn@nus.edu.sg

**Rajeev K. Jaiman \***

Department of Mechanical Engineering  
National University of Singapore  
Singapore  
Email: mperkj@nus.edu.sg

### **ABSTRACT**

A numerical investigation of vortex-induced vibration (VIV) of a pair of identical circular cylinders placed side by side in an uniform flow has been performed. One of the cylinder is elastically mounted and only vibrates in the transverse direction, while its counterpart remains stationary. When two cylinders are placed sufficiently close to each other, a flip-flopping phenomenon can be an additional time-dependent disturbance in the range of  $0.2 \lesssim g^* \lesssim 1.2$ . This phenomenon was well-reported by the experimental work of Bearman and Wadcock [1] in a side-by-side circular cylinder arrangement, in which the gap flow biased toward one of the cylinders and switched the sides intermittently. Albeit one of the two cylinders is free to vibrate, this flip-flopping during VIV dynamics can still be observed. In the side-by-side arrangement, the lock-in region shrinks due to the presence of its stationary counterpart and occurs prematurely compared to that of an isolated counterpart. Similar to the tandem cylinder arrangement, in the post lock-in region, the vibration amplitude is amplified compared to the isolated counterpart. For the vibrating cylinder in the side-by-side arrangement, the biased gap flow shows a quasi-stable flow regime within the lock-in region, instead of a bi-stable regime which is reported in the stationary side-by-side arrangement. When these factors take place simultaneously, the dynamics of freely vibrating cylinder becomes complex and such a side-by-side canonical arrangement is common in offshore engineering applications, for example a floating platform operating in the side of FPSO, arrays of riser

and pipelines, ships travelling in rows within close proximity and many other side-by-side operations. The chaotic fluctuation and large vibration may occur when two bluff bodies are placed closely. It often causes inevitable damages and potential risks to the offshore structures and may leads to a collision or long-term fatigue failure associated with flow-induced vibrations.

### **1 INTRODUCTION**

Offshore structures exhibit a great variety of flow-induced vibrations, which pose severe challenges to the design and operation due to the occurrence of large amplitudes and loads. When the structure is free to vibrate in transverse direction, a strong non-linear coupling between the motion of structure and the wake vortices exists. This results in a complex evolution of the shedding frequency which deviates from the Strouhal law as the natural frequency of the structure is approached, which is referred to as a lock-in of the vortex shedding frequency to the structural frequency [2]. The lock-in range corresponds to a large amplitude oscillatory motion of the bluff body, which is of a practical importance in offshore and marine structures [3,4]. In most offshore engineering applications, multiple structures are far more common than an isolated structure. The flow patterns and forces are strongly dependent upon the arrangement and the distances between these multiple structures [5]. Furthermore, there is a considerable difference between the fluid-structure coupled response of an isolated cylinder arrangement and multiple cylinder arrangements due to the complex effects of vortex-to-

---

\*Address all correspondence to this author.

vortex, vortex-cylinder and gap flow interactions. Of particular interest in this work is to understand the dynamics of side-by-side interactions, we consider the flow around two cylinders in both stationary and vibrating conditions as an idealized model.

Many experimental and numerical investigations have been performed on the isolated circular cylinder and multiple circular cylinders [5] in arrangement [6–8], side-by-side arrangement [9, 10] and staggered arrangement [11]. Vortex-induced vibration (VIV) is one of the important factors causing failures and drawing research interest for improving design and performance of offshore structures. For instance, in the offshore oil and gas engineering, two subsea pipelines or risers are sometimes strapped together to form a coupled two-pipe system. In such a circumstance, the flow-induced vibrations in a cross-flow problem caused by the adjacent cylinders are critical and complicated to deal with, especially when flip-flopping phenomenon is involved. During the flip-flopping instability in the gap flow regime, the jet flow could not maintain its straight pathline and the jet has a tendency to deflect intermittently. This phenomenon was reported in the pioneering works of Ishigai et al. [12], Bearman and Wadcock [13], Williamson [14] and Kim and Durbin [15]. It was noticed that the wake behind the side-by-side circular cylinder arrangement was asymmetric and the gap flow between the two cylinders was biased either upwards or downwards in the range of  $0.2 \lesssim g^* \lesssim 1.2$ .

To analyse the interaction between gap flow and VIV, it is important to different interference types in the steady cross-flow problem. Generally speaking, the interferences in cross-flow problem of cylinders can be classified into two categories, namely proximity interference and wake interference [5]. In the wake interference, the nearby cylinders are downstream and further away from the near-wake region of the upstream one. Those wakes provide periodic perturbations (vorticity and turbulence) upstream of the nearby cylinders and influence (superimpose over each other) the wakes of the nearby cylinders. This is particularly important in the tandem and staggered arrangements. While in the proximity interference ( $g^* \lesssim 2.7$ ), the presence of the other bluff bodies affects the vortex formation and vortex-shedding process of the one under investigation, here  $g^*$  is the ratio of spacing between the cylinder surfaces to the diameter of the diameter. Therefore, the influence on the dynamics of the structure is very significant. As a result, the numerical investigations in present work are limited between  $g^* = 0.5 - 2.5$  in which the proximity-interference ( $0.0 \lesssim g^* \lesssim 2.7$ ) and flip-flopping phenomenon ( $0.2 \lesssim g^* \lesssim 1.2$ ) occur simultaneously. During the bistable flip-flopping condition, the disparate values of force coefficients, Strouhal number and the phase angles can be found experimentally on the cylinders and one of the cylinder exhibits a narrow wake and the other one shows a wide wake [15].

The vortex-induced vibration of a circular cylinder near a stationary wall has been recently studied by Tham et al. [16], in which the dynamics of the isolated cylinder is subjected to

the proximity-interference and the gap flow due to the nearby stationary wall. As an analogous case where two cylinders are placed in a side-by-side arrangement, the proximity interference imposes different dynamical characteristics, which leads to a change in the trend of the vibration amplitude of the cylinder with respect to the reduced velocity. As reported by Tham et al. [16], the streamwise oscillation was enhanced as compared to that in an isolated cylinder case, due to the influence of boundary layer from the stationary wall. A third response branch was also found within the lock-in region. On the contrary, in a side-by-side arrangement, the flip-flopping and periodically shedded vortices from nearby cylinder are additional interferences to the flow field. The exit stream of the flow through the cylinder-cylinder gap and cylinder-wall behaves differently, whereby the existing jet of the side-by-side cylinders shows the oscillatory pattern involving a bistable deflection along the centerline location. It is noteworthy that the existing experimental studies of the proximity interference are conducted at higher Reynolds number. In our previous studies [8, 16], it was shown that the essential aspects of the fluid-structure interaction and VIV dynamics can be analyzed numerically at lower  $Re$ .

The present study focuses on the numerical investigation of the flip-flopping interference due to the gap flow on the VIV of one of the side-by-side cylinders which is free to vibrate in a transverse direction. Ishigai et al. [12, 15] reported that the biased gap flow between two stationary circular cylinder is bistable and changes direction intermittently through a strong bimodal distribution. Our numerical study is based on the two questions about the coupled stability exchanges between the VIV dynamics and gap flow behaviour. Is there a connection exists between the gap flow with the lock-in resonance? How the vortex synchronization process will affect the gap flow in the vibrating condition? It is known that the flip-flopping is highly sensitive bistable phenomenon, and is directly related to interaction dynamics of the coherent vortex patterns with the jet passing through the gap between the cylinders. To analyze the interaction dynamics and the couple stability exchanges, we employ recent data analysis techniques namely, Hilbert-Huang Transformation (HHT) [17] and Sparsity-promoting Dynamic Mode Decomposition (SPDMD) [18]). They are able to decompose the complex Data sets and analyze their temporal information, for instance instantaneous phase angle and frequency, influential modes and decay/growing rate and amplitude. In the present work, HHT is used to analyze the phase angle relationships among variables to study the net energy transfer. Through the SPDMD technique, the dominant modes will be identified to study the stability of flow field and investigate the temporal behaviours of wake dynamics.

## 2 Numerical Methodology

### 2.1 Governing equation

A numerical scheme implementing Petrov-Galerkin finite-element and semi-discrete time stepping is adopted in the present work to investigate the interactions of incompressible viscous flow and rigid-body dynamics. The incompressible Navier-Stokes equations is used in the arbitrary Lagrangian-Eulerian (ALE) reference frame and formulated in the following form

$$\rho^f \left( \frac{\partial \mathbf{u}^f}{\partial t} \Big|_{\hat{x}} + (\mathbf{u}^f - \mathbf{w}) \cdot \nabla \mathbf{u}^f \right) = \nabla \cdot \boldsymbol{\sigma}^f + \mathbf{b}^f \text{ on } \Omega^f(t), \quad (1)$$

$$\nabla \cdot \mathbf{u}^f = 0 \text{ on } \Omega^f(t), \quad (2)$$

where  $\mathbf{u}^f = \mathbf{u}^f(\mathbf{x}, t)$  and  $\mathbf{w} = \mathbf{w}(\mathbf{x}, t)$  are the fluid and mesh velocities respectively. In Eq. 1, the partial time derivative with respect to the ALE referential coordinate  $\hat{x}$  is constant.  $\mathbf{b}^f$  represents the body force per unit mass and  $\boldsymbol{\sigma}^f$  is the Cauchy stress tensor for a Newtonian fluid which is defined as

$$\boldsymbol{\sigma}^f = -p\mathbf{I} + \mu^f \left( \nabla \mathbf{u}^f + (\nabla \mathbf{u}^f)^T \right). \quad (3)$$

where  $p$ ,  $\mu^f$  and  $\mathbf{I}$  are the hydrodynamic pressure, the dynamic viscosity of the fluid and an identity tensor respectively.

The formulation of two dimensional rigid-body motion in Cartesian Coordinate System is shown below,

$$\mathbf{m} \cdot \frac{\partial \mathbf{u}^s}{\partial t} + \mathbf{C} \cdot \mathbf{u}^s + \mathbf{k} \cdot (\boldsymbol{\varphi}^s(\mathbf{z}_0, t) - \mathbf{z}_0) = \mathbf{F}^s + \mathbf{b}^s \quad \text{on } \Omega^s, \quad (4)$$

where  $\mathbf{m}$ ,  $\mathbf{C}$ ,  $\mathbf{k}$ ,  $\mathbf{F}^s$  and  $\mathbf{b}^s$  are mass, damping coefficient and stiffness coefficient vectors for the translational motions, fluid traction and body forces on the rigid body respectively.  $\Omega^s$  represents the domain occupied by the rigid body.  $\mathbf{u}^s(t)$  represents velocity of immersed rigid body.

The new position of rigid body is updated through an position vector  $\boldsymbol{\varphi}^s$ , which maps the initial position  $\mathbf{z}_0$  of the rigid body to its new position at time  $t$ . Let  $\gamma$  be the Lagrangian point on  $\Gamma$  and its corresponding mapping position vector to the new position after motion of rigid body is  $\boldsymbol{\varphi}(\gamma, t)$  at time  $t$ . Since position and flow field around moving rigid body is updated continuously, the no-slip and traction continuity conditions should be satisfied on the fluid-body interface  $\Gamma$ ,

$$\mathbf{u}^f(\boldsymbol{\varphi}^s(\mathbf{z}_0, t), t) = \mathbf{u}^s(\mathbf{z}_0, t), \quad (5)$$

$$\int_{\boldsymbol{\varphi}(\gamma, t)} \boldsymbol{\sigma}^f(\mathbf{x}, t) \cdot \mathbf{n}^f d\Gamma + \int_{\gamma} \mathbf{F}^s d\Gamma = 0 \quad \forall \gamma \in \Gamma, \quad (6)$$

where  $\mathbf{n}^f$  and  $\mathbf{n}^s$  are defined as the normal surface vectors pointing into the fluid.

A partitioned iterative scheme based on a nonlinear interface force correction [19] is used to solve the fluid-rigid body interaction. The temporal discretization of both the fluid and the structural equations is formulated in the generalized- $\alpha$  framework by making use of classical Newmark approximations in time which was proposed by J. Chung and G.M. Hulbert [20]. The velocity and pressure are updated via the restarted Generalized Minimal Residual (GMRES) solver proposed in Y. Saad and M.H. Schultz [21]. The GMRES uses a diagonal preconditioner and a Krylov space of 30 orthonormal vectors. In the current formulation, Newton-Raphson type iterations are implemented to minimize the linearization errors per time step. For the sake of completeness, we next present our post-processing techniques to analyze the complex interactions between gap flow and VIV dynamics.

### 2.2 Dynamic mode decomposition

To analyze the wake flow structures, the dynamic mode decomposition (DMD) is used to explore various temporal information of the complex dataset as a time sequence of velocity fields [22]. A SVD-based DMD technique, Sparsity-promoting Dynamic Mode Decomposition (SPDMD), is incorporated, which allows to flexibly identify the dominant modes based on emphasis/least-square penalty on the different energy level of each DMD modes [18]. In contrast to the classical FFT, the SPDMD analysis is useful to identify the behaviour of the different time frequencies occurring during the interaction of the gap flow with the side-by-side wakes. The essential algorithm of SPDMD is given as follows:

1. Take time-sequential snapshots of the flow field and sort the dataset into two matrices where the columns store values of field variables and the rows contain the data sets collected in each sampling time. The two matrices of snapshots are defined as follow

$$\Phi_0^{n-1} := [\theta_0, \theta_1 \dots \theta_{n-1}] \quad (7)$$

$$\Phi_1^n := [\theta_1, \theta_2 \dots \theta_n] \quad (8)$$

It was postulated that the two time snapshots are in linear relationship and written as

$$\Phi_1^n = A \Phi_0^{n-1} \quad (9)$$

2. Computing SVD of  $\Phi_0^{n-1}$  as

$$\Phi_0^{n-1} = U \Sigma V^* \quad (10)$$

where  $U$  is  $m \times n$  (measurement points)  $\times n$  (number of time series),  $\Sigma$  is  $n \times n$  diagonal matrix and  $V$  is a  $m \times n$  matrix, and  $n$  is the rank of the matrix  $\Phi_0$ .

3. Define the optimal rank- $n$  matrix of  $A$  as

$$F_{dmd} = U^* \Phi_0^n V \Sigma^{-1} \quad (11)$$

4. Solve for the eigenvectors and eigenvalues of  $F_{dmd}$

$$Y_{dmd}^{-1} F_{dmd} Y_{dmd} = E_{dmd}(\mu_n) \quad (12)$$

where  $\mu_n$  is the  $n^{\text{th}}$  eigenvalue of DMD mode and the modes are defined as

$$\kappa = U Y_{dmd} \quad (13)$$

5. The growth/decaying rate and rotational frequency are obtained as

$$\text{Growth/decaying rate} = \text{real}(\log(E_{dmd})) \quad (14)$$

$$\text{rotational frequency} = \text{imag}(\log(E_{dmd})) \quad (15)$$

6. The optimal amplitude of each DMD mode,  $x_{dmd}(\alpha)$ , are obtained by minimizing the least square deviation between the matrix snapshot  $\Phi_0^{n-1}$  and the linear combination of the DMD modes. This is formulated as

$$\underset{\alpha}{\text{minimize}} \quad J(\alpha) := \|\Phi_0^{n-1} - \kappa \text{diag}(x_{dmd}) V_{and}\|_F^2 \quad (16)$$

where  $V_{and}$  is the Vandermonde matrix of  $E_{dmd}$

7. At this stage, the standard SVD-based DMD algorithm is elaborated and the linear approximation of dataset can be written as

$$\underbrace{[\theta_1, \theta_2, \dots, \theta_n]}_{\Phi_0^{n-1}} \approx \underbrace{[\kappa_1, \kappa_2, \dots, \kappa_n]}_{\kappa} \underbrace{\begin{bmatrix} \alpha_1 & 0 & 0 \\ 0 & \dots & 0 \\ 0 & 0 & \alpha_n \end{bmatrix}}_{\text{diag}(x_{dmd})} \underbrace{\begin{bmatrix} 1 & \mu_1 & \dots & \mu_1^{n-1} \\ 1 & \mu_2 & \dots & \mu_2^{n-1} \\ \vdots & \vdots & \ddots & \vdots \\ 1 & \mu_n & \dots & \mu_n^{n-1} \end{bmatrix}}_{E_{dmd} := V_{and}} \quad (17)$$

where  $\kappa$  is DMD mode matrix,  $\text{diag}(x_{dmd})$  is optimal amplitude of each DMD mode and  $E_{dmd}$  is the eigenvalues of  $F_{dmd}$  which describes the temporal behaviours (growth/decay rate and frequency) of each DMD mode.

8. The above steps elaborate the standard SVD-based DMD. Next SPDMD is introduced to select dominant subset of DMD modes through penalizing the non-zero amplitude DMD modes by

$$\underset{\alpha}{\text{minimize}} \quad J(\alpha) + \xi \text{card}(\alpha) \quad (18)$$

where  $\xi$  is the manually specified sparsity range and **card** denotes cardinality function with the  $L_1$ -norm of the vector  $\alpha$ . For this convex optimization problem in the SPDMD process, one can flexibly identify the most influential DMD modes by specifying the sparsity range. With the aid of the Hilbert Transformation, the phase angle of the original signal can be computed from the function  $M_i(t)$  which consists of information of amplitude and local phase.

### 2.3 Hilbert-Huang transformation (HHT)

Fast Fourier Transform (FFT) analysis can analyze a steady and time-invariant signal. It has been considered as a classical signal analytical technique. However, its limitations are also obviously mentioned. Flip-flopping causes a random switching of gap flow, in which frequency and amplitude of aerodynamic variables are changing over time. FFT is not able to analyse these signals/data sets in this case any more. On the other hand, HHT can decompose the unsteady and time-invariant signals and reveal their instantaneous information (e.g., instantaneous amplitude and frequency) regardless of the time-variant characteristics of original signal. HHT consists of two primary analytical techniques. Empirical Mode Decomposition (EMD) decomposes the original signal into different modes (intrinsic mode functions, IMF) through a recursive subtraction process of IMFs from the original signal, sifting process. This sifting process is controlled by a standard deviation. These resultant IMFs are time-variant (instantaneous frequency and amplitude are not constant with respect to time) signals. Following EMD, these intrinsic mode functions are undergone Hilbert Transform (HT) which converts a real signal into its corresponding analytical signals. These intrinsic mode functions in EMD are prepared for HT analysis so as to return the accurate information of the signal. The basic steps of HHT are demonstrated as follow

1. Identify local extrema and link them to form an envelope which are spline fitted.
2. Find the mean values among each pair of local maximum and minimum. These mean values are connected to form a

signal and subtracted from the original signal. Repeat this step until the mean-value formed signal satisfies the definition of IMF.

3. Define this signal as  $IMF_1$  and subtract it from the original signal and repeat step 2 to find the rest of the IMFs

4. Implement Hilbert Transformation on each IMF to explore the temporal information of the original signal. The corresponding analytical signals of each IMF is shown as

$$Z_i(t) = A_i(t) + jB_i(t) = M_i(t)e^{j\Psi_i(t)} \quad (19)$$

where  $M_i(t)$  and  $\Psi_i(t)$  are the amplitude and phase angle, respectively.  $A_i$  and  $B_i(t)$  are the  $i^{\text{th}}$  IMF and its corresponding Hilbert Transform respectively.  $B_i(t)$  is shown below

$$B_i(t) = \frac{1}{\pi} Q \int_{-\infty}^{\infty} \frac{A_i(\tau)}{t - \tau} d\tau \quad (20)$$

where  $Q$  is the principal value.

5. As a result, the original signal can be decomposed into the summation of IMFs as

$$A(t) = Re \sum_{n=1}^N M_i(t) \exp[j \int \omega_i(t) dt] \quad (21)$$

where  $\omega_i(t) = \frac{d}{dt} [\Psi_i(t)]$  is the rotational frequency.

### 3 Problem definition and convergence study

The schematic diagram of a flow across two identical circular cylinders in side-by-side arrangement is illustrated in Fig. 1. The top cylinder (Cylinder1) is mounted on spring-damper system and can vibrate in transverse direction (1DOF), whereas the bottom cylinder (Cylinder2) remains stationary. The flow direction is parallel to the  $x$ -axis from the left toward the right of domain.  $L_u$ ,  $L_d$  and  $H$  represent the upstream distance, the downstream distance and the height of domain respectively. The upper and lower boundaries of the domain are defined as slip-wall boundary condition. A uniform freestream velocity,  $U = 1.0$ , is defined on inlet. At the outlet boundary, a traction-free Neumann boundary condition is prescribed. Apart from the gap ratio  $g^*$ , the flow-induced vibration of the side-by-side is affected by

the following parameters

$$m^* = \frac{4M}{\rho^f \pi D^2} = 10 \quad (22)$$

$$Ur = \frac{U_\infty}{f_n D} \in [2, 10] \quad (23)$$

$$\zeta = \frac{C}{4\pi M f_n} = 0.01 \quad (24)$$

$$Re = \frac{U_\infty D}{v} = 100 \quad (25)$$

$$St = \frac{f_{vs} D}{U_\infty} \quad (26)$$

where  $m^*$ ,  $\rho^f$ ,  $M$ ,  $D$ ,  $f_n$ ,  $f_{vs}$ ,  $\zeta$ ,  $C$ ,  $Re$ ,  $St$  and  $v$  are mass ratio, density of fluid, mass per unit length of cylinder, diameter of cylinder, structural frequency, vortex shedding frequency, damping ratio, damping coefficient, Reynolds number, Strouhal number and kinematic viscosity, respectively. The peak amplitude  $A_y^{\max}$  in the transverse direction is defined as  $A_y^{\max} = \sqrt{2} A_y^{\text{rms}}$ . The size of computational domain is 100D (50D upstream; 50D downstream)  $\times$  100D (cross flow direction), which is sufficiently large to reduce the effects of the artificial boundary conditions defined around the fluid domain. The computational mesh around cylinders is shown in Fig. 2. Two pairs of diagonal lines are drawn in the domain around cylinders. These lines are used to control the exact number of nodes around essential position in the domain so as to further refine the particular near wake region. A mesh dependence study is shown in Table 1. The mesh MSH2 is adopted in the present study, since it confirms the adequacy of the numerical results.

All numerical results obtained from the time convergence

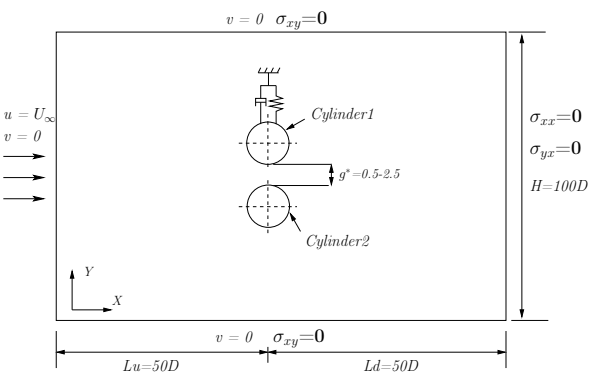


**FIGURE 1:** Schematic diagram of side-by-side cylinders and associated boundary condition details. The top cylinder (Cylinder1) is free to vibrate in transverse direction.

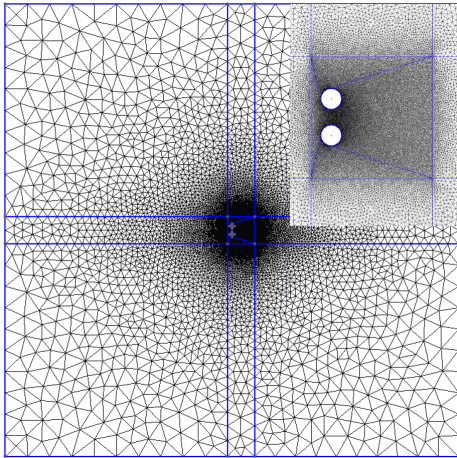


**FIGURE 2:** Representative mesh distribution of side-by-side arrangement at  $g^* = 0.8$

**TABLE 1:** Mesh independent study

Mesh	MSH1	MSH2	MSH3
$\Delta t$	0.02	0.02	0.02
$N_{cyl}$	68	120	180
$N_e$	24,854	50,588	101,956
$C_d^{mean}$	1.434 (0.4%)	1.429 (0.8%)	1.440
$C_L^{mean}$	0.180 (3.4%)	0.175 (0.6%)	0.174
$C_l^{rms}$	0.267 (2.6%)	0.260 (0%)	0.260
$St$	0.162 (1.8%)	0.162 (1.8%)	0.165

\* $N_{cyl}$ : number of points around each cylinder;  $N_e$ : total number of elements in the domain;  $Re=100$ ,  $g^*=1.5$ , stationary cylinders in side-by-side arrangement

study (Table 2) show a very small deviation among each other. The time step  $\Delta t = 0.02$  is adopted in the present study. The percentage of differences in the quantities are listed in the parenthesis.

In order to validate the adopted numerical scheme, a comparison of numerical results from literatures are listed in Table 3. These numerical investigations are performed for the stationary circular cylinders in side-by-side arrangement at  $Re=100$ ,  $g^*=1.5$ . Observing from Table 3, the hydrodynamic coefficients and Strouhal number have a good agreement with the reported results of Kang [23] and Carini [24].

**TABLE 2:** Time convergence study

Time Step	$C_d^{mean}$	$C_l^{mean}$	$C_l^{rms}$	$St$
$\Delta t = 0.08$	1.430 (0.1%)	0.172 (2.3%)	0.2639 (1.1%)	0.165 (1.8%)
$\Delta t = 0.04$	1.429 (0%)	0.176 (0%)	0.261 (0%)	0.162 (0%)
$\Delta t = 0.02$	1.429 (0%)	0.175 (0.6%)	0.260 (0.4%)	0.162 (0%)
$\Delta t = 0.01$	1.429	0.176	0.261	0.162

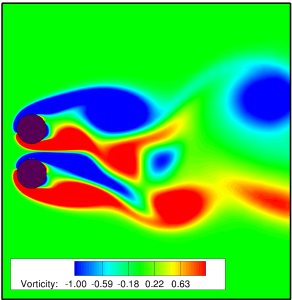
**TABLE 3:** Assessment of hydrodynamic properties for side-by-side cylinders: the mean value of drag coefficient ( $C_d^{mean}$ ), the maximum fluctuation of lift coefficient ( $C_l^{max}$ ) Strouhal number ( $St$ )

	$C_d^{mean}$	$C_l^{max}$	$St$
Kang [23]	1.434 (0.3%)	0.271 (0.4%)	0.164 (1.2%)
Carini [24]	1.409 (1.42%)	0.262 (3.8%)	0.163 (0.6%)
Present	1.429	0.272	0.162

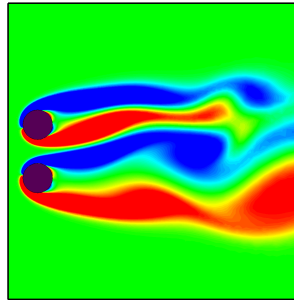
## 4 Results and Discussion

### 4.1 Stationary side-by-side arrangement

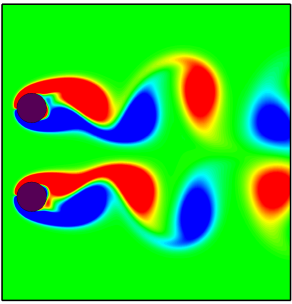
When a pair of identical cylinders are placed side by side in a uniform flow, a range of flow regimes appear at different  $g^*$ . For  $g^* \lesssim 0.2$ , the flow regime around these two cylinders behaves like a single bluff body. For larger gaps  $3.7 \lesssim g^*$ , the wake consists of two separate vortex streets from each cylinder and there is a weak coupling between the wakes. These two vortex streets synchronize and become anti-phase to each other at most of the time. However, these two Karman vortex streets still remain its symmetry and shed at identical frequency, which can be observed in Figs. 3c and 3d. If the gap ratio is small enough ( $g^* < 1 - 1.2$ ), the biased gap flow can be observed in the side-by-side arrangement, which is shown in Figs. 3a and 3b. There is a net lift force on each cylinder which repels its counterpart and points to the opposite directions, which can be attributed to the movement of the two stagnation points. This has a similarity with the case of near-wall arrangement [16]. As the gap ratio increases, the values of these two lift forces approach each other and eventually become closer to that of isolated circular cylinder case. This trend is illustrated in Fig. 4. Due to the existence of flip-flopping phenomenon, the fluctuation of lift force is very irregular. It can be observed from Figs. 4a and 4b that in the transition stage fluctuation of lift forces are still regular before  $t^* \lesssim 30$ . It is the occurrence of flip-flopping that causes irregular



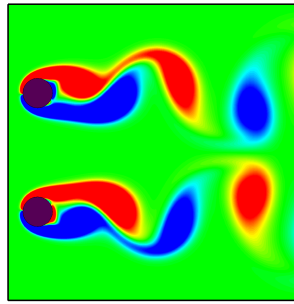
(a)



(b)



(c)

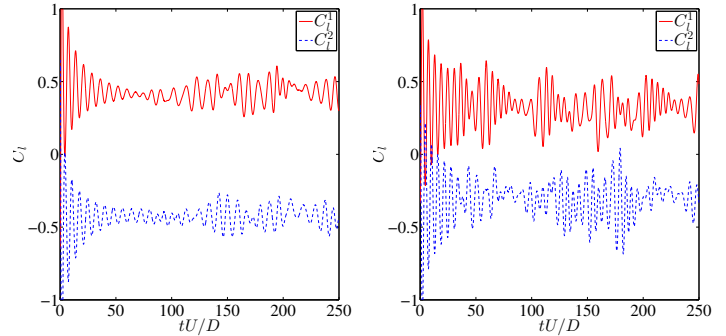


(d)

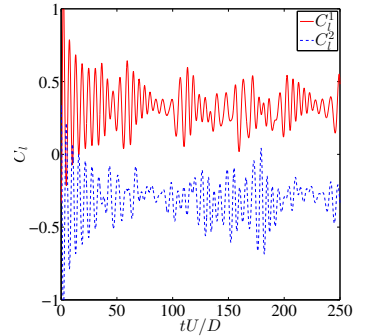
**FIGURE 3:** Contour plots of stationary cylinders in side-by-side arrangement for the gap flow mode: (a)  $g^* = 0.5$ , (b)  $g^* = 0.8$ ; coupled vortex flow: (c)  $g^* = 2.0$ , (d)  $g^* = 3.0$

alternation of phase angles of the lift forces. This flip-flopping of gap flow was reported by Kim and Durbin [15]. It is observed that the gap flow behaves between two quasi-stable states which occurs at a random frequency. The cylinder with the deflected jet flow has a narrower near wake region.

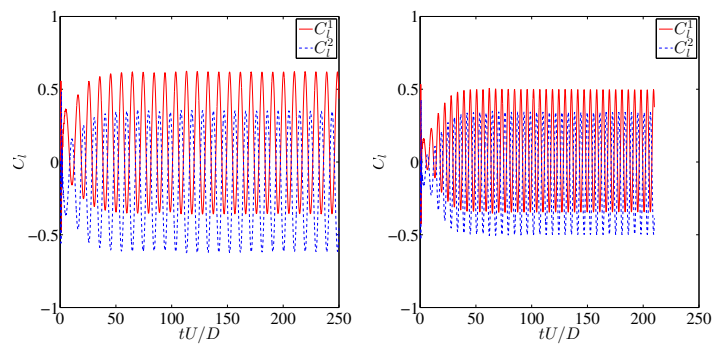
Recently, it was reported by Carini et al. [24] that there was a very low-frequency unstable Floquet mode which caused by the occurrence of flip-flopping phenomenon of gap flow and shifting of instantaneous phase angle during the interaction of side-by-side wake structures. Thereafter, the switching between in-phase and anti-phase of fluctuation of fluid forces occurs periodically. In present study, to investigate the phase angle change over time, the Hilbert-Huang transformation is implemented to quantify the instantaneous phase angles of each variable. The results are plotted in Fig 5, which shows the time history of the instantaneous phase angle deference between  $C_d$  (Fig 5d) and the  $C_l$  (Fig. 5c) of the two cylinders. For illustration purpose, the phase angle difference ( $\beta$ ) is defined in the first and second quadrants. It can be seen that during the initial transition stage the  $C_d$  of both cylinders are in-phase. After the occurrence of flip-flopping, the anti-phase mode is dominant. In terms of lift



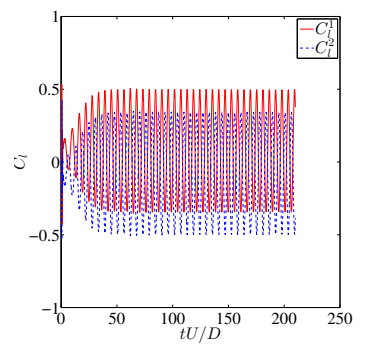
(a)



(b)



(c)



(d)

**FIGURE 4:** Time history of  $C_l$  variation of stationary cylinders in side-by-side arrangement for the gap flow mode: (a)  $g^* = 0.5$ , (b)  $g^* = 0.8$ ; and the coupled vortex: (c)  $g^* = 2.0$ , (d)  $g^* = 3.0$

forces, during the initial stage, the  $C_l$  are anti-phase. This is also observed in the cases of larger gap ratio ( $g^* > 1 - 1.2$ ). Due to the flip-flopping phenomenon, the switching between in-phase and anti-phase fluctuation is very frequent. It is obvious that this irregularity is caused by the flip-flopping phenomenon and it does not have a well-defined frequency. In the next section, the simultaneous occurrence of the vortex-induced-vibration and the flip-flopping phenomenon is investigated to understand a possible synchronization of the biased gap-flow in a vibrating side-by-side arrangement.

## 4.2 Vibrating side-by-side arrangement

In the side-by-side arrangement, if one of the cylinders experiences the vortex-induced vibration (VIV), the biased gap flow shows a different behaviour while  $U_r$  is within the lock-in region. To the best of our knowledge, the interaction of flip-flopping and VIV is not reported in the literature for this arrangement. In present study, the biased gap flow clings to the side of vibrating cylinder while the vortex-shedding frequency of the vibrating cylinder is close to the structural frequency of itself (lock-in

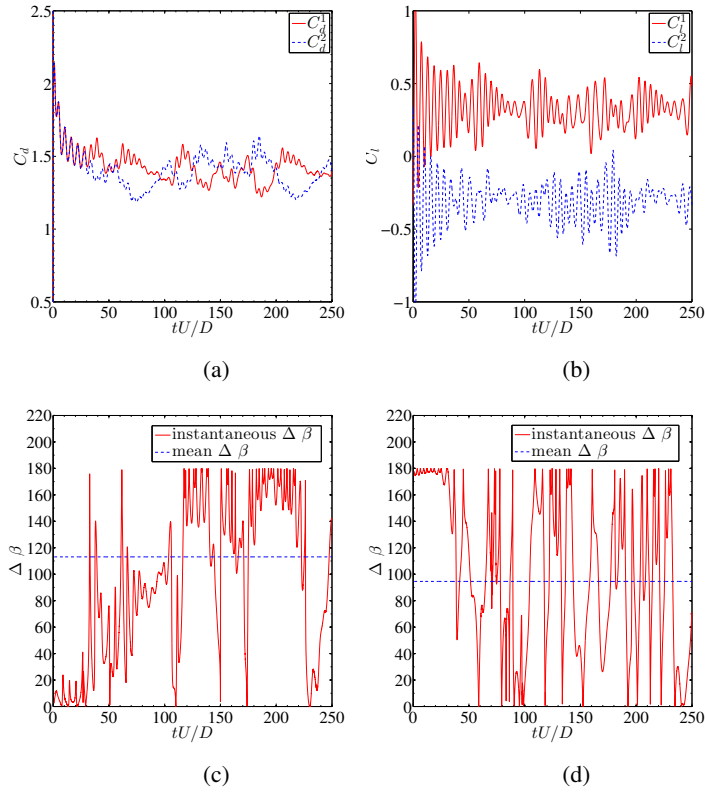


**FIGURE 5:** Time history of instantaneous phase angle difference between (a,c)  $C_d$ , (b,d)  $C_l$  of stationary cylinders in side-by-side arrangement ( $Re = 100$ ,  $g^* = 0.8$ ). Here  $\beta$  represents the difference in the phase angle.

region). This is shown in the representative contour plots of various  $Ur$  in Fig. 6.

To confirm this observation, investigations of  $\beta$  of the vibrating side-by-side arrangement is performed and the results are shown in Fig. 7. It shows that the phase angle differences between  $C_d$  and  $C_l$  of the two cylinders are approximately  $0^\circ$  and  $90^\circ$ , respectively after the occurrence of flip-flopping. This can be further analyzed through the Sparsity-promoting Dynamic Mode Decomposition of vorticity. In Fig. 8, the most influential nine DMD modes ( $Re=100$ ,  $g^*=0.5$ ,  $Ur=5$ ) are presented. The more influential modes are marked with red crosses and have a relative higher amplitude value,  $\alpha$ . The corresponding DMD mode vorticity contour plots are shown in Fig. 10. As seen from Figs. 10a and 10b, the DMD modes at Strouhal number 0 and 0.9 are rather symmetric; on the contrary, DMD modes in Figs. 10c and 10d are asymmetric and cling to the vibrating cylinder. The DMD modes of vorticity which biased toward the stationary cylinder are not strong enough to be observed in the present analysis or do not exist. It is also shown in Fig. 9 that all these selected more influential DMD modes are very stable (the insta-

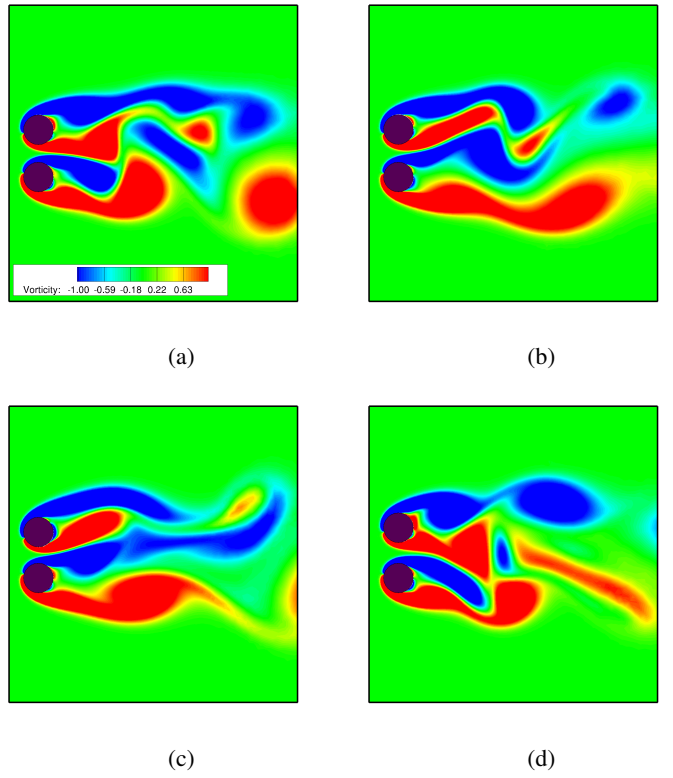


**FIGURE 6:** Contour plots of 1-DOF vibrating cylinder in side-by-side arrangement at  $g^* = 0.6$  for  $Ur = (a)2, (b)4, (c)6, (d)8$

ble mode is outside the unit circle and stable mode should lay on the unit circle). Therefore, it can be confirmed that the gap-flow indeed biases toward the vibrating cylinder in a quasi-stable manner within lock-in region. This phenomenon can also be explained from Figs. 12 and 13. In Fig. 12, when  $Ur$  falls outside the lock-in region, the vibration of cylinder is not significant and  $C_d^{mean}$  on two cylinders are almost identical. When  $Ur$  is within the region of lock-in, the vibrating cylinder always has a higher value of  $C_d^{mean}$ . This could be due to the narrower near wake region caused by biased-over gap flow. This is analogous to the case of side-by-side stationary cylinders. Fig. 13 shows that  $C_l^{rms}$  from both cylinders are almost identical to each other when  $Ur$  is outside lock-in region. The difference between  $C_l^{rms}$ 's only amplifies during lock-in region in which the gap flow always biases toward one direction and causes asymmetric  $C_l^{rms}$ . Besides the investigation of gap flow, it is also found that the lock-in region becomes narrower and occurs earlier than the isolated counterpart. It is observed that the gap flow passes through the gap and bends towards the vibrating cylinder. This biased gap flow makes the near wake region of corresponding cylinder narrower and enhances interaction of the free shear layers shedded from both side of cylinder. As a result, the frequency of vortex

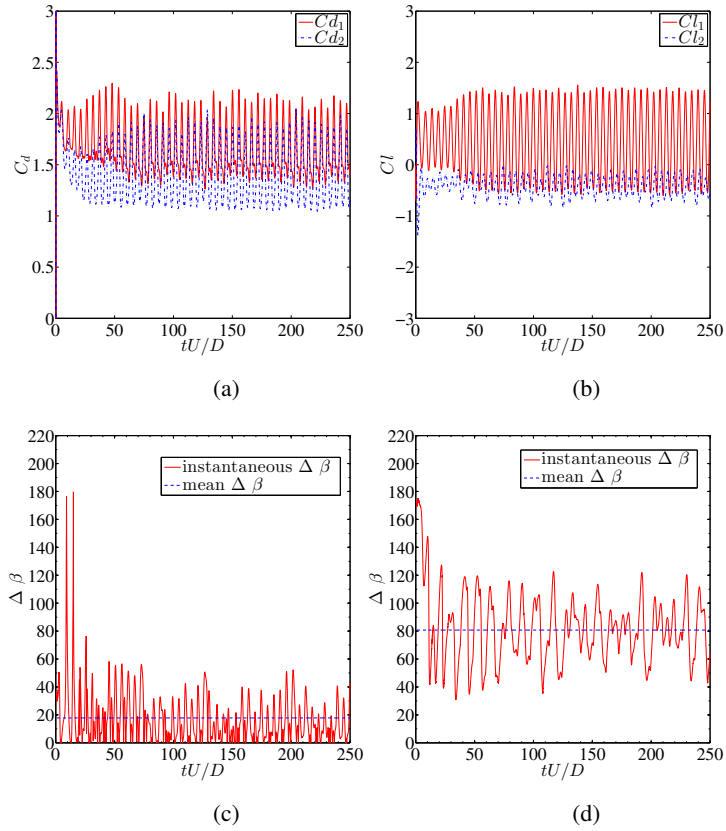


**FIGURE 7:** Time history of instantaneous phase angle difference between (a,c)  $C_d$ , (b,d)  $C_l$  of vibrating cylinder in side-by-side arrangement ( $Re = 100, g^* = 0.6, Ur = 5$ )

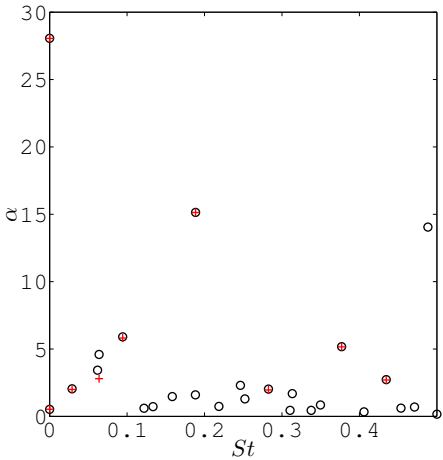


**FIGURE 8:** Relationship between amplitude and frequency through the sparsity-promoting dynamic mode decomposition of vorticity ( $Re = 100, g^* = 0.5, Ur = 5$ , number of DMD mode=9)

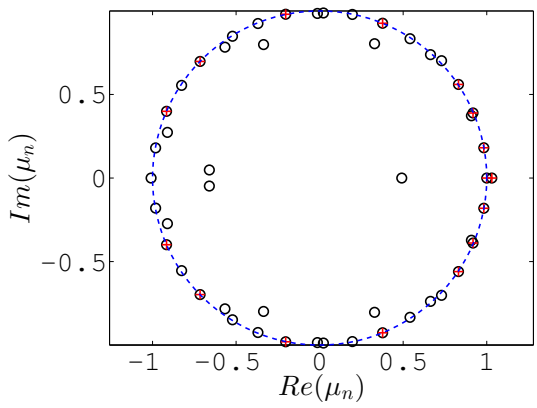


**FIGURE 9:** Stability plot of real( $\mu_n$ ) and imaginary( $\mu_n$ ) eigenvalues through SPDMD analysis of vorticity ( $Re = 100, g^* = 0.5, Ur = 5$ , where the number of DMD modes are 9)

shedding becomes larger than that of the isolated counterpart for the identical  $Ur$  [25]. This trend is shown in Fig. 11. It is discernible that at the same  $Re$  and  $Ur$  values, the vibrating cylinder in present side-by-side arrangement has relative higher frequency compared with that of an isolated transversely-vibrating cylinder. Therefore, at the identical  $Ur$ , the cylinder in the current arrangement experiences an enhanced vortex-shedding frequency and synchronizes earlier with the structural frequency of cylinder. As result, the lock-in starts earlier than the isolated cylinder for the identical reduced velocity. This tendency is shown in Fig. 14. On the contrary, in an analogous near-wall arrangement, since the vortex on the near wall side is inhibited by a stationary wall, the corresponding lock-in region ends later than that of isolated VIV case. This tendency is confirmed through sampling results (Fig. 15) of  $A_y^{max}$  at various  $g^*$  in which biased gap flow occurs. Particularly, at  $g^*=2.5$  where two cylinders are relatively far away from each other, the lock-in region shows a tendency to recover back to the behaviour that of isolated cylinder case.

To understand the interaction between gap flow and downstream wakes, it is better to analyse the streamline plots of both arrangements shown in Fig. 16. In Figs. 16a and 16b, due to the characteristics of the stream function, the gap flow is not able to cross each other to maintain its straight pathline and follows the streamlines' curvature around downstream wakes. In other words, the flow patterns are manifested by gap flow are significantly influenced by the dynamics patterns of the nearby downstream wakes. Therefore, biased gap flow phenomenon may also

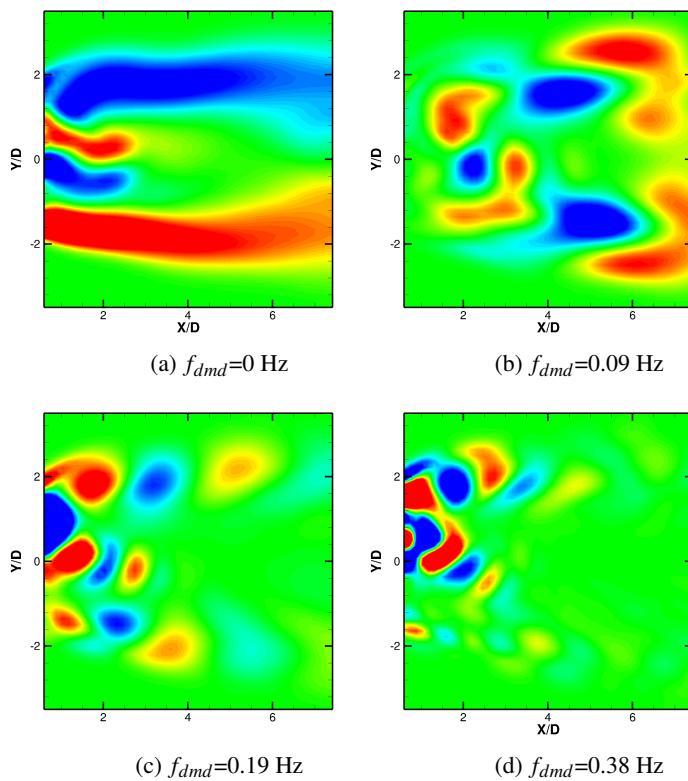


**FIGURE 10:** DMD modes of vorticity for flow in the wake of cylinders in side-by-side arrangement for  $Re = 100$ ,  $g^* = 0.5$ ,  $U_r = 5$ , where Cylinder1 vibrates in transverse direction and  $f_{dmd}$  is the frequency of a DMD mode

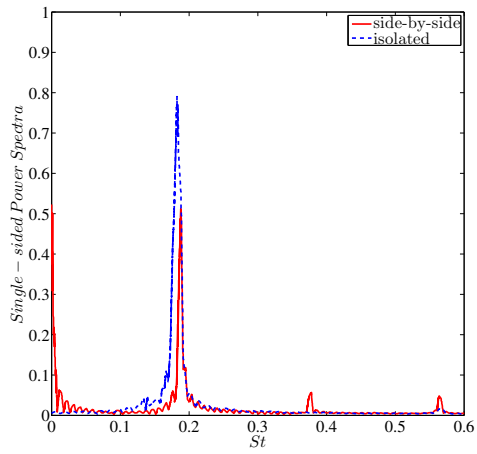


**FIGURE 11:** Fast Fourier Transformation (FFT) analysis of isolated vibrating cylinder and vibrating cylinder in a side-by-side arrangement ( $Re = 100$ ,  $m^* = 10$ ,  $\zeta = 0.01$ ,  $U_r = 5$ )

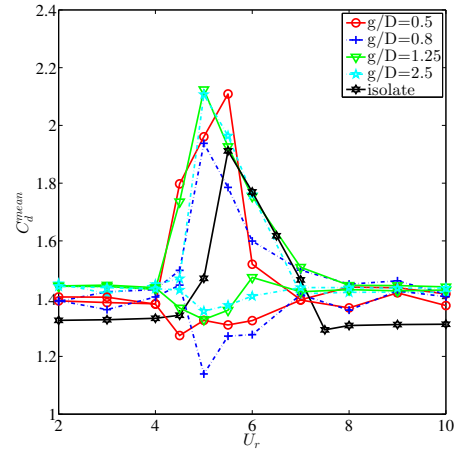


**FIGURE 12:** Relationship between mean drag  $C_d^{mean}$  and reduced velocity  $U_r$  for the side-by-side arrangement ( $Re = 100$ ,  $m^* = 10$ ,  $\zeta = 0.01$ )

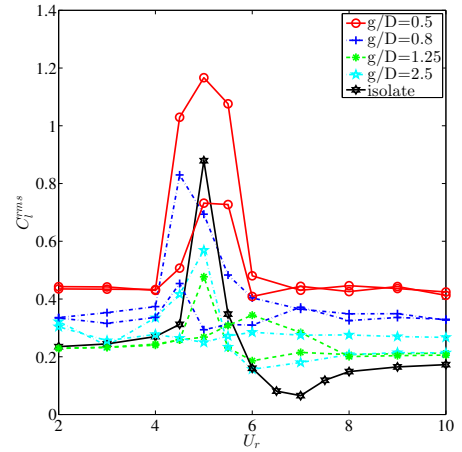


**FIGURE 13:** Relationship between fluctuating lift  $C_L^{rms}$  and reduced velocity  $U_r$  of the side-by-side arrangement ( $Re = 100$ ,  $m^* = 10$ ,  $\zeta = 0.01$ )

be interpreted as a results of the gap-flow and wake interaction. This can be observed clearly from Fig. 16a. There is a four-way saddle point near a large wake and just on the stream direction path of the gap flow. This saddle point locates exactly at the local low velocity (magnitude) region. Once the fluid approaches this particular point, there are four optional paths for that fluid particles can follow. As a result, the gap flow is forced to change its course from the straight path and biased toward one side. On the contrary, as shown in Fig. 16b, 4-way saddle point on the

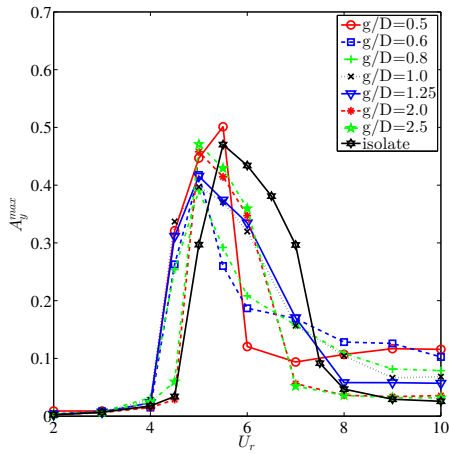


**FIGURE 14:** Dependence of  $A_y^{\max}$  on  $U_r$  for side-by-side arrangement ( $Re = 100, m^* = 10, \zeta = 0.01$ )

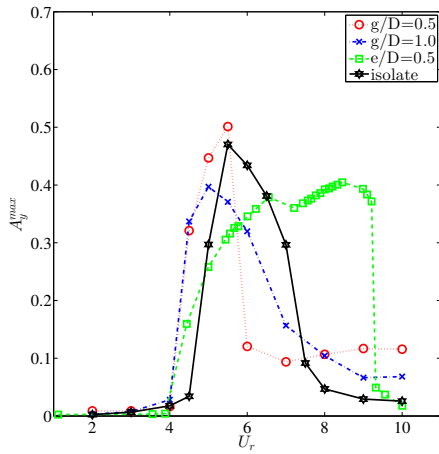


**FIGURE 15:** Comparison of peak amplitude  $A_y^{\max}$  as a function of  $U_r$  for the side-by-side and near-wall arrangements for  $Re = 100, m^* = 10, \zeta = 0.01$ . Here  $e/D$  denotes the gap from the stationary wall.

middle path of gap flow, which is generated by large wakes is not observed in vibrating side-by-side arrangement within lock-in region, is not observed. It probably shed light on how the gap-flow bias toward the vibrating cylinder quasi-stably in side-by-side arrangement.

## 5 CONCLUSIONS

The present study investigated the effect of the interaction of the flip-flopping, vortex-induced vibration and gap flow

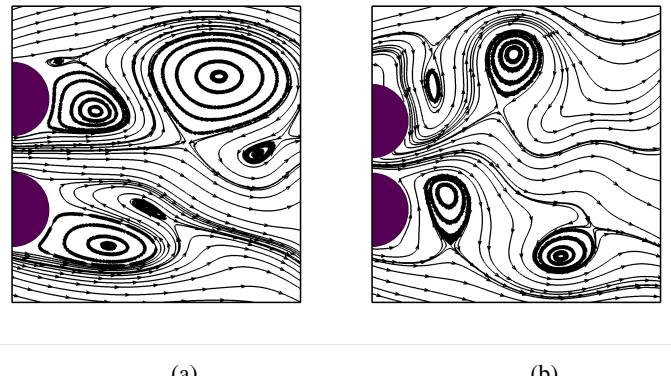


**FIGURE 16:** Streamline plots of cylinders in side-by-side arrangement ( $Re=100, g^*=0.5$ ) (a) stationary, (b) vibrating ( $U_r=5$ )

interaction on a side-by-side circular cylinders arrangement, whereby one cylinder is stationary and the other vibrates in the transverse direction. This interaction was analysed through the amplitude response, the phase angle relationship study, the modal analysis, and the wake flow visualizations. In the phase angle relationship, it was shown that the flip-flopping originated a series of irregular instantaneous phase angle shifts in the coupled wake dynamics. Due to the flip-flopping of the gap flow, the phase angle differences of drag and lift coefficients were found to vary in-phase and out-phase intermittently without a well-defined frequency. The jet flow passing through the gap was found to be biased toward cylinder vibrating cylinder in the lock-in region and the vibrating cylinder experienced a higher drag force. In the modal analysis by DMD, it was shown that the most influential mode of vorticity were either symmetric in the streamwise direction or stronger on the side of vibrating cylinder. The DMD mode of vorticity which biased toward the side of the stationary cylinder was not observed in the present modal analysis. It was also noticed that the lock-in region occurred earlier and the range of lock-in became narrower. The interaction between two free shear layers from both sides of vibrating cylinder was more frequent and enhanced significantly. Consequently, the corresponding shedding frequency of vibrating cylinder matched structural frequency of immersed body much more earlier than that of the isolated cylinder case. The origin of flip-flopping phenomenon was elaborated through instantaneous streamline plots of both stationary and vibrating side-by-side arrangements. It was shown that there were four-way saddle points formed by strong local vortex wakes along the middle pathline of the gap flow in a side-by-side arrangement of stationary cylinder at  $g^*=1.5$ , such that the gap flow followed its flow path from more than one options and it is unstable. On the other hand, the four-way saddle point were away from the middle path of gap flow in a vibrating side-by-side arrangement.

for  $g^*=0.5, Ur=5$  (lock-in). However due to the asymmetry of downstream wakes still existed, the gap flow biased toward one side of the side-by-side arrangement. In the future, the interactions between flip-flopping and vortex-induced vibration will investigated in detail at high Reynolds number.

**Acknowledgments** The first author would like to thank Singapore Maritime Institute Grant (SMI-2014-OF-04) for the financial support.

## REFERENCES

- [1] Bearman, P., and Wadcock, A., 1973. "The interaction between a pair of circular cylinders normal to a stream". *Journal of Fluid Mechanics*, **61**(03), pp. 499–511.
- [2] Williamson, C., and Govardhan, R., 2004. "Vortex-induced vibrations". *Annu. Rev. Fluid Mech.*, **36**, pp. 413–455.
- [3] Sarpkaya, T., 2004. "A critical review of the intrinsic nature of vortex-induced vibrations". *Journal of Fluids and Structures*, **19**(4), pp. 389–447.
- [4] Bearman, P., 2011. "Circular cylinder wakes and vortex-induced vibrations". *Journal of Fluids and Structures*, **27**, pp. 648–658.
- [5] Zdravkovich, M., 1987. "The effects of interference between circular cylinders in cross flow". *Journal of fluids and structures*, **1**(2), pp. 239–261.
- [6] Lin, J.-C., Yang, Y., and Rockwell, D., 2002. "Flow past two cylinders in tandem: instantaneous and averaged flow structure". *Journal of Fluids and Structures*, **16**(8), pp. 1059–1071.
- [7] Springer, M., Jaiman, R., Cosgrove, S., and Constantinides, Y., 2009. "Numerical modeling of vortex-induced vibrations of two flexible risers". In ASME Offshore Mechanics and Arctic Engineering OMAE09-79801 CP.
- [8] Mysa, R. C., Kaboudian, A., and Jaiman, R. K., 2016. "On the origin of wake-induced vibration in two tandem circular cylinders at low reynolds number". *Journal of Fluids and Structures*, **61**, pp. 76–98.
- [9] Sumner, D., Wong, S., Price, S., and Paidoussis, M., 1999. "Fluid behaviour of side-by-side circular cylinders in steady cross-flow". *Journal of Fluids and Structures*, **13**(3), pp. 309–338.
- [10] Kang, S., 2003. "Characteristics of flow over two circular cylinders in a side-by-side arrangement at low reynolds numbers". *Physics of Fluids (1994-present)*, **15**(9), pp. 2486–2498.
- [11] Sumner, D., Price, S., and Paidoussis, M., 2000. "Flow-pattern identification for two staggered circular cylinders in cross-flow". *Journal of Fluid Mechanics*, **411**, pp. 263–303.
- [12] ISHIGAI, S., NISHIKAWA, E., NISHIMURA, K., and CHO, K., 1972. "Experimental study on structure of gas flow in tube banks with tube axes normal to flow: Part 1, karman vortex flow from two tubes at various spacings". *Bulletin of JSME*, **15**(86), pp. 949–956.
- [13] Bearman, P., and Wadcock, A., 1973. "The interaction between a pair of circular cylinders normal to a stream". *Journal of Fluid Mechanics*, **61**(03), pp. 499–511.
- [14] Williamson, C., 1985. "Evolution of a single wake behind a pair of bluff bodies". *Journal of Fluid Mechanics*, **159**, pp. 1–18.
- [15] Kim, H., 1988. "Investigation of the flow between a pair of circular cylinders in the flopping regime". *Journal of Fluid Mechanics*, **196**, pp. 431–448.
- [16] Tham, D. M. Y., Gurugubelli, P. S., Li, Z., and Jaiman, R. K., 2015. "Freely vibrating circular cylinder in the vicinity of a stationary wall". *Journal of Fluids and Structures*, **59**, pp. 103–128.
- [17] Huang, N. E., Shen, Z., Long, S. R., Wu, M. C., Shih, H. H., Zheng, Q., Yen, N.-C., Tung, C. C., and Liu, H. H., 1998. "The empirical mode decomposition and the hilbert spectrum for nonlinear and non-stationary time series analysis". In Proceedings of the Royal Society of London A: Mathematical, Physical and Engineering Sciences, Vol. 454, The Royal Society, pp. 903–995.
- [18] Jovanovic, M. R., Schmid, P. J., and Nichols, J. W., 2014. "Sparsity-promoting dynamic mode decomposition". *Physics of Fluids (1994-present)*, **26**(2), p. 024103.
- [19] Jaiman, R., Pillalamarri, N., and Guan, M., 2016. "A stable second-order partitioned iterative scheme for freely vibrating low-mass bluff bodies in a uniform flow". *Comput. Methods Appl. Mech. Engrg.*, **301**, pp. 187–215.
- [20] Chung, J., and Hulbert, G., 1993. "A time integration algorithm for structural dynamics with improved numerical dissipation: the generalized- $\alpha$  method". *J. Appl. Mech.*, **60**, pp. 370–375.
- [21] Saad, Y., and Schultz, M., 1986. "Gmres: A generalized minimal residual algorithm for solving non-symmetric linear systems". *SIAM Journal on Scientific and Statistical Computing*, **7**.
- [22] Schmid, P. J., 2010. "Dynamic mode decomposition of numerical and experimental data". *Journal of Fluid Mechanics*, **656**, pp. 5–28.
- [23] Kang, S., 2003. "Characteristics of flow over two circular cylinders in a side-by-side arrangement at low reynolds numbers". *Physics of Fluids (1994-present)*, **15**(9), pp. 2486–2498.
- [24] Carini, M., Giannetti, F., and Auteri, F., 2014. "On the origin of the flipflop instability of two side-by-side cylinder wakes". *Journal of Fluid Mechanics*, **742**, 3, pp. 552–576.
- [25] Sumer, B. M., and Fredsøe, J., 1997. *Hydrodynamics around cylindrical structures*, Vol. 12. World Scientific.